Sediment characterization of bottom propagating reversing buoyancy particle-bearing jets

Mohnish Kapil,[1] Bruce R. Sutherland,[2,3,*] and Sridhar Balasubramanian[1,4,†]
[1]*Department of Mechanical Engineering, Indian Institute of Technology Bombay, Mumbai, Maharashtra, 400076, India*
[2]*Department of Physics, University of Alberta, Edmonton, Alberta, Canada T6G 2E1*
[3]*Department of Earth & Atmospheric Sciences, University of Alberta, Edmonton, Alberta, Canada T6G 2E3*
[4]*IDP in Climate Studies, Indian Institute of Technology Bombay, Mumbai, Maharashtra, 400076, India*

(Received 1 July 2022; accepted 7 October 2022; published 26 October 2022)

We develop theory and perform laboratory experiments on reversing buoyancy particle-bearing wall jets in a uniform ambient fluid, examining the lofting characteristics of the jet and particle sedimentation. Theoretical considerations involving several parameters predict the lofting location and the deposition pattern. The suction forces present at the bottom wall dominantly influence the lofting location of the jet. The sediment dynamics are influenced by drag at the bottom wall, entrainment of ambient fluid into the jet, and several scale factors involving the settling of the particles. Our theory shows that the ratio of deposit width to length depends on the jet's drag coefficient and entrainment dynamics. Experimentally, we find that this ratio is higher when the particle concentration is large, suggesting that sedimenting particles exert a nonnegligible additional drag on the jet. The results clearly show changes in the jet dynamics brought about by the presence of particles in reversing buoyancy jets.

DOI: 10.1103/PhysRevFluids.7.104302

I. INTRODUCTION

There are numerous incidences in natural and industrial settings where particles suspended in a fluid of one density intrude into a fluid of another density (e.g., volcanic eruptions, hydrothermal vents, turbidity currents, and effluent discharge). The flows of particular interest here are initially horizontal propagating particle-bearing currents or jets, in which the interstitial fluid is lighter than the ambient fluid. However, dense particles in the flow make the bulk density higher than the ambient fluid density. These are referred to as reversing buoyancy currents [1,2]. As the flow evolves, the particles gradually rain out, reducing the bulk density. When the flow becomes less dense than the ambient fluid, the flow rises upward at a lift-off point through a process known as lofting. Such flows occur naturally, for example, as reversing buoyancy pyroclastic flows [3] and lofting turbidity currents [1,2,4,5] and as a consequence of offshore waste discharge [6].

Studies of reversing buoyancy currents have focused predominantly on the run-out length of a lock-release buoyancy current (see, e.g. [1,2,5,7]). Sparks *et al.* [1] examined lock-release experiments on reversing buoyancy currents showing that the sediment deposit pattern exhibits an abrupt decrease in its thickness beyond the lift-off point. Hogg *et al.* [2] used shallow water theory to predict the lift-off location, finding good agreement with their experiments. In a study of particle

*bruce.sutherland@ualberta.ca; https://www.ualberta.ca/~bsuther
†sridharb@iitb.ac.in; http://www.gmfl.in

deposition patterns from lock-release reversing buoyancy currents with a mixture of coarse and fine particles, Gladstone and Pritchard [5] showed a gradual decay in the deposition depth starting from the source, ending sharply near the lofting location for both types of particles. They observed a well-sorted deposition pattern among fine and coarse sediments.

There are few studies on the dynamics and associated sediment deposition patterns of reversing buoyancy currents from constant-flux sources. The study of constant-flux reversing buoyancy currents for a particle-laden current by Hürzeler *et al.* [4] showed that the lateral spreading rate decreases with increasing detrainment of interstitial fluid due to particle settling. They observed the rising of many individual buoyant plumes contrary to the single continuous plume observed in lock-release experiments [1], and they derived spreading relations predicting the lift-off distance using dimensional analysis. A recent experimental study on constant-flux reversing buoyancy particle-bearing currents on a shallow slope by Steel *et al.* [8] showed a narrower width of the sediment deposits than what usually occurs for currents without reversing buoyancy. However, in their study the focus was mainly on the sediment structure and not on the flow and sedimentation dynamics.

Numerical models have been developed to estimate the sediment deposits and grain sorting in constant volume and constant flux reversing buoyancy currents [9]. The results under-predict the front position and the sediment deposit pattern compared with the experiments of Hürzeler *et al.* [4].

The work presented here examines the dynamics and sedimentation from a horizontal particle-bearing jet with relatively buoyant interstitial fluid. This configuration differs from the better-studied problem of a vertical particle-bearing buoyant plume [10–12]. Even in the absence of particles, there are only a few studies on buoyant jets emanating horizontally from a localized source. Abraham [13] used similarity principles to examine the evolution of a buoyant jet in momentum and buoyancy-dominated regions. Hirst [14] derived integral equations for the buoyant jet motion incorporating the effect of buoyancy arising from entrainment using the model of Morton *et al.* [15]. Jirka [16] developed a generalized integral jet model based on flux quantities assuming a Gaussian radial distribution of velocity and density differences with the ambient fluid. Trajectories were well predicted, despite neglecting the jet-wall interactions. Sharp and Vyas [17] also considered the drag and suction forces exerted by the lower boundary upon a wall jet. The inclusion of suction resulted in a delayed downstream rise of the jet trajectory, in good agreement with experimental results. Similar consideration of jet attachment toward the horizontal wall boundary due to suction can be seen in the study of Burridge and Hunt [18].

The experimental study of a non-buoyant particle-bearing jet propagating over the horizontal boundary by Kapil *et al.* [19] showed self-similar jet behavior despite variations in particle concentration up to 1%. The deposition pattern showed a teardrop shape with maximum deposition near the source. That study also showed the influence of bedload transport on the maximum deposition location. In an experimental and numerical study of a horizontal buoyant particle-bearing wall jet by Cuthbertson *et al.* [20], no particle influence on the jet trajectories was observed due to having less than 0.1% particle concentration. The centerline sediment deposition showed significant sediment deposition near the jet source with a gradual decrease in depth farther downstream. Here we extend this study to include the influence of particle concentrations up to 2%, and focus on the sedimentation and deposition patterns formed before and after the jet lofts due to reversing buoyancy.

In Sec. II we describe the theory for lofting particle-bearing jets. In Sec. III we describe the experimental setup, the measurement techniques and the analysis methods. The quantitative results are shown in Sec. IV, and the conclusions are reported in Sec. V.

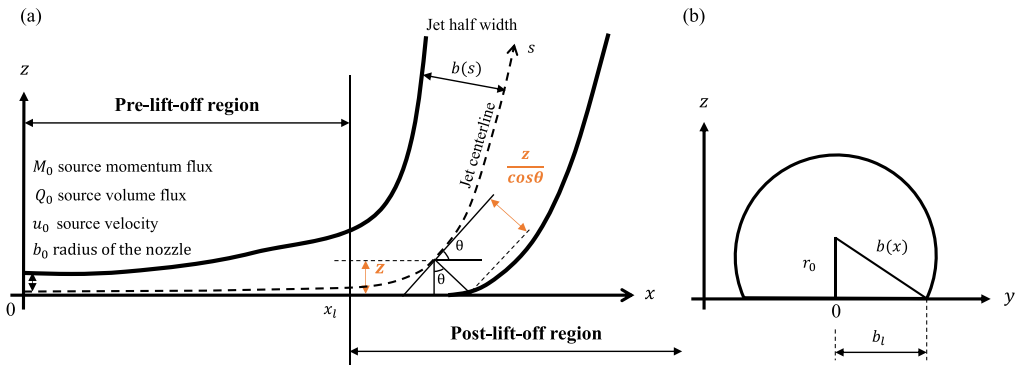

FIG. 1. Schematic of the horizontal wall jet showing (a) the side view and (b) the cross-section view when the jet centerline is oriented at an angle of θ from the horizontal beyond the lofting location.

II. THEORETICAL CONSIDERATIONS

The velocity and reduced gravity are assumed to have a Gaussian distribution in the radial direction from the jet centerline:

$$u(r,x) = u_c(x)e^{-r^2/b(x)^2} \quad \text{and} \quad g'_t(r,x) = g'_{tc}(x)e^{-r^2/b(x)^2} \tag{1}$$

in which $u_c(x)$ is the jet centerline velocity, $b(x)$ is a measure of the jet half-width, g'_{tc} is the total reduced gravity at the jet centerline, and $r^2 = y^2 + z^2$, in which x is the along-jet coordinate, y is the spanwise coordinate, and z is vertical.

The total centerline reduced gravity, g'_{tc} is written into two parts, $g'_{tc} = g'_{ic}(x) - g'_p\phi_c(x)$, with the contribution from the particles having reduced gravity, $g'_p = g(\frac{\rho_p-\rho_a}{\rho_a})$, and the interstitial fluid having reduced gravity, $g'_{ic} = g(\frac{\rho_a-\rho_{ic}}{\rho_a})$, in which $\rho_{ic}(x)$ is the centerline interstitial fluid density and $\phi_c(x)$ is the particle volume fraction at the jet centerline. The density of the particles, ρ_p, ambient fluid, ρ_a, and acceleration due to gravity, g, is constant. Unlike u and g'_t, the particle concentration is assumed to have compact support that decreases quadratically in the radial direction away from the centerline to width $W(x)$:

$$\phi(r,x) = \phi_c(x)(1 - r^2/W^2). \tag{2}$$

The volume, momentum, and particle-volume fluxes are given, respectively, by

$$Q = \iint u\,dA, \quad M = \iint u^2\,dA, \quad \text{and} \quad \Phi = \iint \phi u\,dA \tag{3}$$

in which the integrals are in the cross-sectional y-z plane. For a jet advancing over a horizontal boundary, the values of these fluxes are given explicitly by

$$Q = \frac{\pi}{2}b^2u_c, \quad M = \frac{\pi}{4}b^2u_c^2, \quad \text{and} \quad \Phi = \frac{\pi}{2}b^2u_c\phi_c\left[\left(1 - \frac{b^2}{W^2}\right)(1 - e^{-W^2/b^2})\right]. \tag{4}$$

For a free jet after lofting, which has a circular as opposed to a semicircular cross section, these values are twice as large.

The jet evolution is divided into two regions, as shown in Fig. 1. In the "pre-lift-off region," the jet centerline trajectory follows a horizontal path along the bottom boundary. In the "post-lift-off region," the trajectories become inclined to the horizontal bottom and lofts, eventually becoming a buoyant plume. Equations describing the jet evolution and particle deposition in each region are presented below.

A. Pre-lift-off region

The conservation of volume, adapted from [15] for a wall jet, is given by

$$\frac{dQ}{dx} = \pi \alpha u_c b(x), \tag{5}$$

where α is the entrainment coefficient.

We assume the momentum of the jet is influenced by drag exerted by the boundary over which it propagates [17,21]. Hence, the conservation of horizontal momentum is given by

$$\frac{dM_x}{dx} = -C_d(2b)u_c^2, \tag{6}$$

where C_d is the drag coefficient.

The similarity solutions for $u_c(x)$ and $b(x)$ of a reversing buoyancy particle-bearing jet using Eqs. (5) and (6) are found to be

$$u_c(x) = x^{-\frac{\alpha\pi+4C_d}{\alpha\pi+2C_d}} \tag{7}$$

and

$$b(x) = \frac{2}{\pi}(\alpha\pi + 2C_d)x. \tag{8}$$

The rate of change of particle volume flux can be estimated by assuming that the particles leave the flow only through the viscous sublayer at the base given by [2,22–24]

$$\frac{d\Phi}{dx} = -\beta w_s \int \phi \, dy. \tag{9}$$

Here β is a factor defining the enhanced particle settling, and w_s is the particle fall velocity. The factor β is added to account for turbulent fluctuations in the Gaussian jet. Equation (9) is used for diagnostic purposes only for the pre-lift-off region. To evaluate the integral of Eq. (9), it is necessary to establish its upper and lower spanwise limits. The lower limit, W_i, accommodating the no particle region near the source due to bedload transport is estimated from the Shield's parameter [19]:

$$W_i = b\left\{\max\left(0, \left[\log\left(\frac{u_c}{u_{Sh}}\right)\right]^{1/2}\right)\right\} \quad \text{in which} \quad u_{Sh} = \sqrt{g'_p d_p}/\gamma_s, \tag{10}$$

where u_{Sh} is the critical velocity below which no bedload transfer occurs, γ_s is an empirical scale factor denoting the end of bedload transport near the source, and d_p is the particle diameter. We use an empirical value of $\gamma_s = 0.3$ from the study of a particle-bearing wall jet in uniform ambient fluid [19]. This applies to our case due to the momentum-dominant nature of the jet near the source.

The upper limit, W, is estimated by assuming that the Gaussian profile of the jet velocity falls below the settling velocity of the particles. Hence, all the particles settle within this width. It is given as

$$W = b\left\{\max\left(0, \left[\log\left(\frac{u_c}{u_{Stl}}\right)\right]^{1/2}\right)\right\} \quad \text{in which} \quad u_{Stl} = \gamma w_s, \tag{11}$$

where u_{Stl} is the empirical fluctuating velocity associated with turbulent eddies at the jet boundary, and γ is a constant scale factor incorporating the effect of these velocity fluctuations.

Using (2) to replace ϕ in Eq. (9) with the above upper and lower limits for width, we get

$$\frac{d\Phi}{dx} = -\beta w_s \int_{W_i}^{W} \phi dy = -\beta w_s \left[\frac{4}{3} W \phi_c - \frac{2}{3} W_i \left(3 - \frac{W_i^2}{W^2}\right)\phi_c\right]. \tag{12}$$

This expression provides the variation of particle volume flux in the streamwise direction.

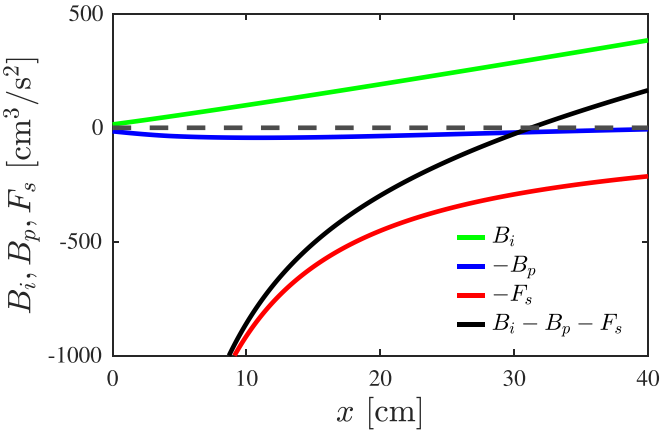

FIG. 2. The evolution of the three components of the forces represented by B_i, B_p, and F_s, influencing the jet lofting [Eq. (13)] with source variables, $Q_0 = 15\,\mathrm{cm}^3/\mathrm{s}$, $\phi_0 = 2\%$, $b_0 = 1.27\,\mathrm{cm}$, $u_0 = 11.8\,\mathrm{cm/s}$, $\frac{\rho_p - \rho_a}{\rho_a} = 1.475$, and $\frac{\rho_a - \rho_i}{\rho_a} = 0.0119$, which are variables corresponding to experiment 6 (see Table I).

B. Lift-off condition

Three forces influence where the jet lifts off: the buoyancy force of the interstitial fluid, the negative buoyancy force due to the presence of the particles, and the suction force resulting from the relatively low pressure of the jet at the bottom boundary [17]. These forces are represented by B_i, B_p, and F_s, respectively. Lift-off occurs when these forces are in balance, and the normal force of the wall on the jet becomes nonnegative:

$$B_i - B_p - F_s = 0 \quad \text{with} \quad B_i = \frac{\pi}{2} b^2 g'_{ic}, \quad B_p = \frac{\pi}{4} W^2 \phi_c g'_p, \quad \text{and} \quad F_s = 2 C_s b u_c^2, \tag{13}$$

in which C_s is the suction coefficient. We denote this horizontal lift-off location by x_l and call it the lift-off point. The contribution from each of the three forces is plotted in Fig. 2 for a particular choice of source conditions given by experiment 6 (see Table I). The sum of forces (represented by the black curve) is negative at the source and gradually increases as the jet moves away from the source. At $x_l \simeq 29\,\mathrm{cm}$, the value crosses zero, which indicates the lift-off point. The contribution from F_s (red curve) dominates the total force near the source, while the contribution of B_p (blue curve) is small. B_i eventually exceeds the suction force away from the source, leading to lift-off.

C. Post-lift-off region

After lift-off, the jet centerline follows a path given by $[x(s), z(s)]$, where s denotes the distance from the source. The direction of the path is given by (see Fig. 1)

$$\frac{dx}{ds} = \cos\theta \quad \text{and} \quad \frac{dz}{ds} = \sin\theta \tag{14}$$

with $\theta = 0^\circ$ for $s \leqslant x_l$

The conservation of volume is given by

$$\frac{dQ}{ds} = a\pi\alpha u_c b(s) \tag{15}$$

in which the value of a gradually changes from 1 for a wall jet to 2 for a free jet during lofting. Explicitly, we take $a = 1 + \min(1, r_0/b)$ in which r_0 denotes the height of the jet centerline from the wall in a plane perpendicular to the jet's path represented by $r_0 = z/\cos\theta$ [see Fig. 1(b)].

TABLE I. Source variables for all the experiments: experiment number (Exp.), particle volume fraction (ϕ_0), particle diameter (d_p), volume flux (Q_0), interstitial fluid density (ρ_i), ambient density ρ_a, bulk particle-fluid density ρ_b, and buoyancy flux, $B_0 = \frac{\pi}{4} g'_{1c} b_0^2 u_0$. Negative values of B_0 indicate the jet is negatively buoyant at the source due to the presence of particles.

Exp.	ϕ_0(%)	d_p	Q_0 (cm^3/s)	ρ_i (g/cm^3)	ρ_a (g/cm^3)	ρ_b (g/cm^3)	B_0(cm^4/s^3)
1	0	0	15	0.998	1.001	0.998	44
2	0	0	15	0.998	1.005	0.998	103
3	0	0	15	0.998	1.010	0.998	175
4	2	30	15	0.998	1.001	1.028	−398
5	2	30	15	0.998	1.005	1.028	−337
6	2	30	15	0.998	1.010	1.028	−263
7	1.5	30	15	0.998	1.001	1.021	−287
8	1.5	30	15	0.998	1.005	1.021	−227
9	1.5	30	15	0.998	1.010	1.021	−153
10	1	30	15	0.998	1.001	1.013	−177
11	1	30	15	0.998	1.005	1.013	−117
12	1	30	15	0.998	1.010	1.013	−44
13	0.5	30	15	0.998	1.001	1.006	−66
14	0.5	30	15	0.998	1.005	1.006	−8
15	0.2	30	15	0.998	1.001	1.001	0
16	1.5	30	15	0.998	0.998	1.021	−332
17	1	30	15	0.998	0.998	1.013	−222
18	2	30	15	0.998	0.998	1.028	−443
19	0.5	30	15	0.998	0.998	1.006	−111
20	0.2	30	15	0.998	0.998	1.001	−44
21	2	60	15	0.998	0.998	1.028	−443
22	2	60	15	0.998	1.001	1.028	−398
23	2	60	15	0.998	1.005	1.028	−337
24	2	60	15	0.998	1.010	1.028	−263
25	1.5	60	15	0.998	0.998	1.021	−332
26	1.5	60	15	0.998	1.001	1.021	−287
27	1.5	60	15	0.998	1.005	1.021	−227
28	1.5	60	15	0.998	1.010	1.021	−153
29	1	60	15	0.998	0.998	1.013	−221
30	1	60	15	0.998	1.001	1.013	−177
31	1	60	15	0.998	1.005	1.013	−117
32	1	60	15	0.998	1.010	1.013	−44
33	0.5	60	15	0.998	0.998	1.006	−111
34	0.5	60	15	0.998	1.001	1.006	−66
35	0.5	60	15	0.998	1.005	1.006	−7
36	0.2	60	15	0.998	0.998	1.001	−44
37	0.2	60	15	0.998	1.001	1.001	0

The momentum of the jet has both a horizontal component, M_x, and a vertical component, M_z. The horizontal momentum equation (6) is modified to account for the jet not being flush with the wall:

$$\frac{dM_x}{ds} = -2C_d b_l u_l^2 \tag{16}$$

in which b_l is the jet width touching the bottom during the initial stages of lofting: $b_l = \sqrt{\max(0, b^2 - r_0^2)}$.

The vertical momentum equation involves the three forces in Eq. (13), also adapted for $s \geqslant x_l$:

$$\frac{dM_z}{ds} = \pi b^2 g'_{ic} - \frac{\pi}{2} W^2 \phi_c g'_p - 2C_s b_l u_l^2. \tag{17}$$

Here $u_l = u_c e^{-r_0^2/b^2} \cos\theta$ is the speed of the jet at $z = 0$. The rate of change of particle volume flux is given by (9) with x replaced by s, and the integration bounds, W_i and W, remain the same because most particles rain out near the source. In Eqs. (16) and (17), the drag and suction forces eventually vanish once the jet lifts off entirely from the bottom.

D. Sedimentation

The sediment deposit is assumed to accumulate particles over time as they leave the jet while settling on the bottom boundary. The accumulated volume of particles and sediment depth can be calculated using the loose packing fraction for spheres, p_f. Explicitly, using Eq. (9) the rate of change of sediment depth is $\frac{dh}{dt} = \frac{1}{p_f} \beta w_s \phi$, where $p_f = 0.56$. For the total duration of the experiment, t_f, the final sediment depth takes the form

$$h(x, y) = \frac{1}{p_f} \beta w_s \phi t_f, \quad \text{where} \quad \phi = \phi_c(x) \left(1 - \frac{y^2}{W^2(x)}\right). \tag{18}$$

We define L_s as the distance between the runout location, X_m, (the streamwise distance where sediment deposition is zero) and the location, X_{W_s}, where the spanwise deposition width is maximum. From the theory above, L_s is given analytically by

$$L_s = X_m - X_{W_s} = \frac{b_0}{2\alpha(1+p)} \left(\frac{2u_0}{\gamma w_s}\right)^{\frac{1+p}{1+2p}} (1 - e^{-1/2}), \tag{19}$$

in which $p \equiv 2C_d/(\pi\alpha)$. The maximum deposition width, W_s, is given by

$$W_s = b_0 \left(\frac{2u_0}{\gamma w_s}\right)^{\frac{1+p}{1+2p}} e^{-1/2} \left(\frac{1+2p}{2(1+p)}\right)^{1/2}. \tag{20}$$

Interestingly, the aspect ratio W_s/L_s takes the following form:

$$\frac{W_s}{L_s} = \frac{\sqrt{2}\alpha}{e^{1/2} - 1} [(1+2p)(1+p)]^{1/2}, \tag{21}$$

which depends upon only two parameters through the definition of p: α and C_d. If we take $\alpha = 0.16$ and $C_d = 0.02$, as used for our experiments, then $W_s/L_s = 0.39$ is a constant, independent of the source volume flux, particle size, and concentration. This suggests a fixed eccentricity of the sediment shape.

E. Model parameters and results

Here we discuss the influence of each model parameter on the flow evolution and the pattern of sediment deposition. The values for the parameters are based on empirical modeling. We have six model parameters that capture the complex physics associated with lofting and sedimentation. The entrainment parameter, α, captures its influence on the evolution of jet trajectories and the final sediment deposit shape. Increasing the value of α results in early lift-off and a higher aspect ratio, W_s/L_s, of the deposition. The best-fit value of α in our experiments is found to be 0.16, which is higher than that for an unbounded jet $\alpha = 0.075 \pm 0.05$ and a negatively buoyant jet, $\alpha = 0.057$ [25]. However, recent studies on wall jets and wall plumes have reported higher values of entrainment, specifically, $\alpha_{wj} = 0.0778$ for wall jets and $\alpha_{wp} = 0.110$ for wall plumes [18,21].

The value of C_d plays an important role in modeling the lift-off location. A higher value of drag results in greater decay of horizontal momentum [as seen in Eq. (6)], thereby causing an earlier

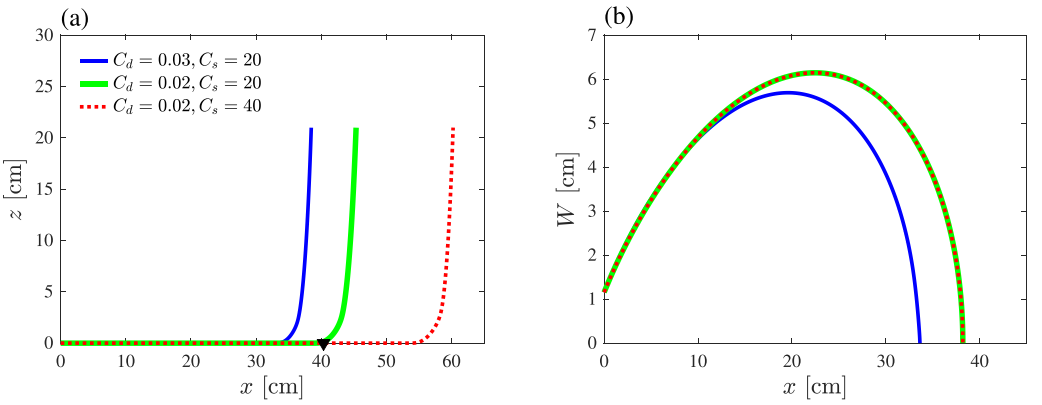

FIG. 3. (a) Theoretical jet centerline trajectories having different C_d and C_s parameters with variables corresponding to experiment 6 shown in Table I. The symbol ▼ corresponds to experimentally observed lofting location of mean jet trajectory. (b) The corresponding width of the sediment deposit, W, as given by Eq. (11); all the curves in (b) have the same parameters and color scheme as (a).

lift-off [see Fig. 3(a)]. The value of C_d also influences W_s/L_s given by Eq. (21): higher C_d results in larger W_s/L_s, corresponding to a more circular deposit [see Fig. 3(b)]. It is generally observed that, for a wall jet, the drag is an order of magnitude higher than the conventional values ($C_d = 0.001$) for a flat plate [21]. For the best comparison to our experiments, we have chosen a value of $C_d = 0.02$ in all our theoretical predictions.

The suction coefficient, C_s, plays a crucial role in accurately determining the lofting location within acceptable error limits [see Fig. 3(a)]. From Fig. 2 we see that the suction force is the dominant parameter that determines whether the jet will remain attached to the surface or not. Therefore the value of C_s has to be appropriately chosen to model this force. The value of the suction coefficient is chosen as $C_s = 20$, based on our experimental lofting locations.

The parameters governing the spanwise extent of sediment deposit are β, γ_s, and γ. The sediment's inner and outer shape involves the parameters γ_s and γ, respectively. Turbulence fluctuations influence these parameters in the near and far field as the jet widens from the source. The parameter β also accounts for the influence of turbulence upon enhanced particle settling through eddies, in part rapidly advecting particles towards the bottom viscous boundary layer. The sediment governing parameters have values $\gamma = 12$ and $\gamma_s = 0.3$ which best predict the experimentally observed sediment deposition pattern (shown later). The enhanced settling scale factor, β, is chosen as $\beta = 5$ in our model.

Figure 4 shows the theoretical predictions of the sediment deposition for two values of C_d. The sediment shape is similar to that of an ellipse. The sediment deposit in both Figs. 4(a) and 4(b) shows elevated sediment deposition at the lofting location. This elevated sediment deposition is essentially the contribution of all the particles lofting nearly vertically at that location. As a consequence of instantaneous particle fallout at the lofting location, a large deposit can be seen in Figs. 4(a) and 4(b) at location $x \simeq 34$ cm and $x \simeq 40$ cm respectively, the corresponding lift-off locations. No such trend in the deposit is observed in our experiments. This is because the horizontal velocity of the jet at the lofting location is sufficient to prevent such a build-up. We would like to emphasize that the values chosen for the six model parameters used in our theory are maintained constant for comparison with all experiments.

III. EXPERIMENTAL SETUP AND ANALYSIS METHODS

Here we describe the apparatus used for performing the experiments along with the techniques used for data analysis.

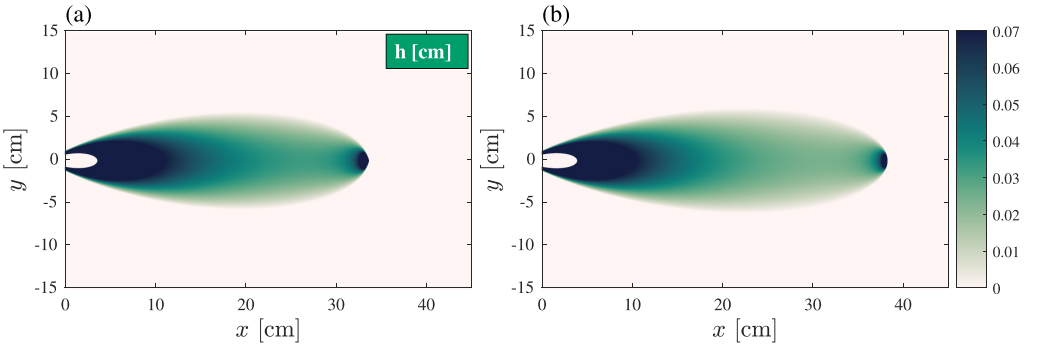

FIG. 4. The theoretical sediment deposit pattern as given by Eq. (18) with variables corresponding to experiment 6 and suction coefficient, $C_s = 20$. Panel (a) corresponds to drag coefficient, $C_d = 0.03$, and (b) corresponds to $C_d = 0.02$. The scale to the right shows the sediment depth in cm.

A. Apparatus

A schematic of the experimental setup is shown in Fig. 5. The experiments were performed in a rectangular tank with length $L_T = 90$ cm, width $W_T = 90$ cm, and height $H_T = 45$ cm. Depending upon the experiments, the ambient density ρ_a in the tank varied from $0.998\,\mathrm{g/cm^3}$ to $1.010\,\mathrm{g/cm^3}$. The maximum depth of the fluid in the tank was maintained at 35 cm. The reservoir was a rectangular container with a pyramid-shaped bottom down-sloping at an angle of 30°, with its length $L_R = 45$ cm, width $W_R = 40$ cm, and height $H_R = 30$ cm above the sloping bottom. The reservoir carried the particle-bearing fluid into the tank, through the bottom apex, connected with a ball valve to a flexible hose. A nozzle of radius, $R = 1.27$ cm, was attached to the other end of the hose. It contained a fine mesh of radius 0.2 cm, which ensured a turbulent flow [26]. The nozzle was placed at midplane along the bottom of the tank. The flexible hosing allowed the clamp to adjust the flow rate at the source $Q_0 = \pi b_0^2 u_0$. For our study, a constant value of $Q_0 = 15\,\mathrm{cm^3/s}$ was used giving a Reynolds number $\mathrm{Re} = u_0 b_0/\nu$, a value of 1300. A stirring mechanism consisted of a blade mounted on a stirring rod driven by a motor. This was placed inside the reservoir in order for the particles to remain suspended. Since the bottom of the reservoir was 100 cm above the tank, it established a near-constant pressure flow from the reservoir. In order to generate the lofting jets, the

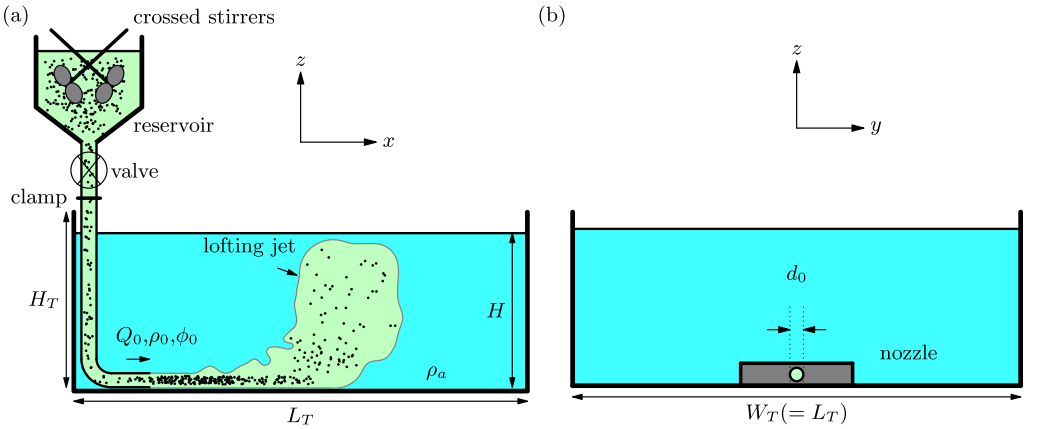

FIG. 5. Schematic of the experimental setup showing (a) the side view and (b) the front view with nozzle.

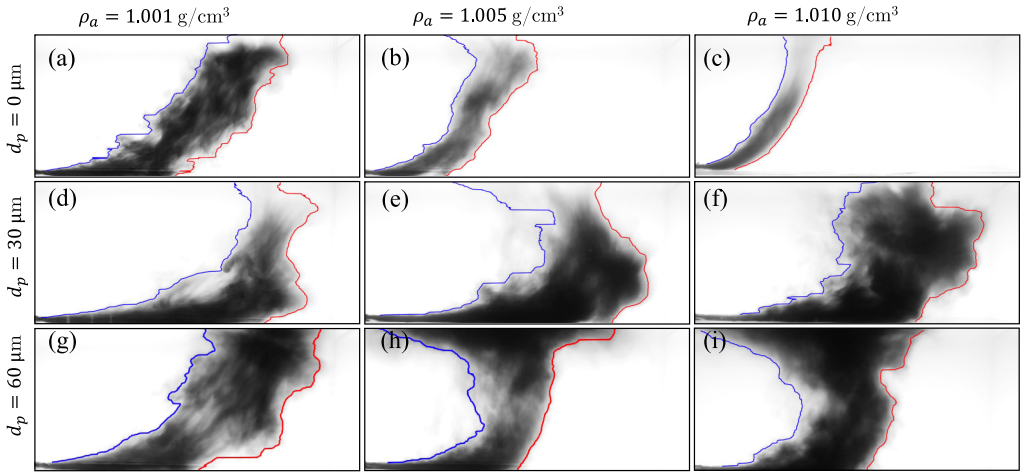

FIG. 6. Propagation of the jet with and without particles having different ambient densities ρ_a, particle concentration, ϕ_0, and diameter, d_p. Panels (a)–(c) refer to experiments 1, 2, and 3, respectively, and show the jet without any particles. Panels (d)–(f) show the particle-bearing jet with particle diameter, $d_p = 30\,\mu$m, and refer to experiments 15, 11, and 6 having particle concentration, $\phi_0 = 0.2\%$, 1%, and 2%, respectively. Panels (g)–(i) refer to experiments 37, 31, and 24, having $\phi_0 = 0.2\%$, 1%, and 2%, respectively, with particle diameter, $d_p = 60\,\mu$m. All the snapshots have dimensions length = 80 cm and height = 35 cm.

fluid used in the reservoir was tap water, and saltwater was used in the tank (tap water mixed with industrial-grade salt). The maximum depth of the fluid in the reservoir was maintained at 20 cm.

Before each experiment, the stirrer was allowed to mix the fluid inside the reservoir. It was followed by adding 20 ml of blue dye and the measured quantity of the glass particles having a density $\rho_p = 2.5\,\mathrm{g/cm^3}$. Two different particle diameters were used, having a mean diameter of either $d_p = 30 \pm 10\,\mu$m or $d_p = 60 \pm 15\,\mu$m. Careful measurement of the mass and size of the particles and the initial volume of water inside the reservoir ensured a prescribed source volume concentration, ϕ_0 of the particles. We have chosen the concentration in terms of the volume fraction of the particles, ϕ_0, within the 0–2% range. If the concentration of the particles was high and the density difference between ambient and interstitial fluid was low, the jet propagated without any lofting to the end of the tank. In most experiments, the source density of the particle-fluid mixture was higher than the ambient fluid density. This ensured that the flow became a bottom propagating buoyant jet that lofts once the particles settled out. Given the physical constraints in the size of the tank and complex particle-fluid mixture interaction, the source momentum $M_0 = \pi b_0^2 u_0^2$ was sufficiently low to allow for lofting to occur before the jet reached the end of the tank. All the experiments were recorded with the help of two digital cameras (Canon EOS 7D and Canon EOS 1500D) that were placed such that one of them recorded a side view and the other a top-down view.

Table I lists the relevant parameters of all the experiments performed in this study. The consistency of the experiments performed was checked by repeating several experiments as many as three times.

B. Qualitative analysis of the lofting jet

Snapshots from nine experiments of lofting jets are shown in Fig. 6. The edges of the jet are determined by taking the 20% threshold of the maximum intensity of the dye captured by the digital camera during the experiments. Figure 6(a) shows the case of a horizontal jet without particles in a weakly buoyant ambient fluid ($\rho_a = 1.001\,\mathrm{g/cm^3}$) with a jet profile gradually rising some distance away from the source. In a moderately buoyant ambient fluid ($\rho_a = 1.005\,\mathrm{g/cm^3}$) the jet rises closer

to the source with steeper trajectories after lift-off [Fig. 6(b)]; for a strongly buoyant ambient fluid ($\rho_a = 1.010\,\mathrm{g/cm^3}$) the jet lofts close to the source [Fig. 6(c)]. This is expected since the jet becomes more positively buoyant as the ambient density is increased. Figures 6(d)–6(f) show the lofting jet with the same corresponding strengths of buoyancy as in Figs. 6(a)–6(c), but the jet contains particles with diameter $d_p = 30\,\mu$m. With particle concentration, $\phi_0 = 0.2\%$, and weak buoyancy [Fig. 6(d)] the jet stays attached to the bottom over a longer distance compared to the case with no particles [Fig. 6(a)]. As soon as the particles rain out, the jet instantaneously lofts at a location that we call the "lofting point." At particle concentration, $\phi_0 = 1\%$, and moderate buoyancy [Fig. 6(e)] the jet moves farther downstream due to a relatively high concentration of particles before lofting. The observed broader jet profile suggests higher entrainment of surrounding fluid compared to the case with no particles [Fig. 6(b)]. At $\phi_0 = 2\%$, the jet travels a longer distance before lofting in spite of having a strong buoyancy [Fig. 6(f)], this is due to the high concentration of particles at the source, which allows particles to remain further downstream within the jet. The bottom row comprising Figs. 6(g)–6(i) contains the same corresponding strengths of buoyancy and particle concentration as that for Figs. 6(d)–6(f), but the jet contains particles having diameter $d_p = 60\,\mu$m. In a weak buoyancy [Fig. 6(g)] we observe that the jet travels farther than the no particle case but lofts earlier than with the case of particle diameter $d_p = 30\,\mu$m [Fig. 6(d)]. This is due to the large size of the particles present in the jet, wherein most of the particles settle close to the source, and we get a gradual rise of the jet again after moving a considerable distance from the source. With moderate buoyancy, the particles sediment within the length of the jet's propagation. The jet quickly comes to rest in the horizontal direction and instantaneously rises upwards due to the excess positive buoyancy. Finally, with strong buoyancy, the jet starts to rise early before it comes to a complete stop in the horizontal direction, owing to particles settling closer to the source. This suggests that there are upper limits in choosing the size of the particles in order for it not to lose all the particles near the source. We can see that the reversing buoyancy particle-bearing jet follows different propagation dynamics than the jet without particles. The quantitative dynamics of reversing particle-bearing jets, including particle settling and deposition, are presented in detail in Sec. IV.

C. Light attenuation technique

We used a nonintrusive light attenuation method [10,27] to measure the sediment depth at the end of each experiment. In this method, a light source (typically a light-emitting diode panel) was placed beneath the transparent tank bottom. A downward-pointed digital camera (Canon EOS 1500D) was placed at 90 cm above the tank bottom surface. The camera captured and recorded the light intensity, $I_0(x, y)$, before the start of the experiment when there were no particles present. Due to the accumulation of particles on the tank bottom, the intensity of light reaching the camera was reduced. The light intensity I is expected to decrease exponentially [27] with the sediment height h, given by the relation

$$I = I_b + (I_0 - I_b)e^{-h/\sigma_h}. \tag{22}$$

Here I_b is the black intensity, denoting the complete blockage of light by the particles, and σ_h is the e-folding depth denoting the height for which the intensity difference is decreased by e. A calibration tank of length 11 cm and width 11 cm and a block of height 1 cm within it was placed in the main tank. Particles were then added to the calibration tank and were scraped to form a uniform slope of particles with known height and length. The calibration measurements were recorded and processed using MatLab. The intensity versus known height was analyzed to give a best-fit estimate of the three empirical values of I_0, I_b, and σ_h. Given these, the height of the sediment, $h(x, y)$, was determined for the given intensity using Eq. (22). Different calibrations for different particle diameters and ambient fluid were performed. In general, the parameters were relatively insensitive to ρ_a. This method successfully measured the sediment depth within a 5% experimental error.

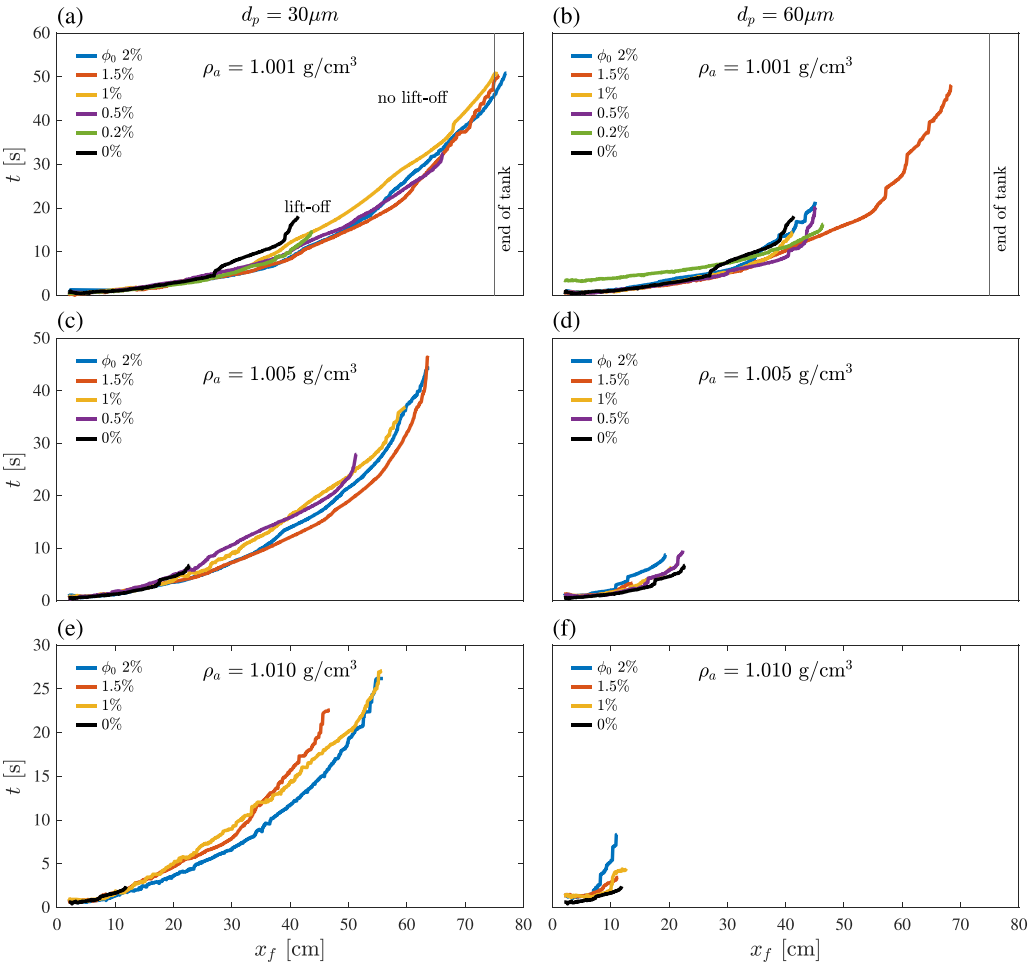

FIG. 7. Front propagation of the jet as it evolves in time. Panels (a), (c), and (e) refer to 30 μm size particles, while panels (b), (d), and (f) refer to 60 μm particles.

IV. QUANTITATIVE RESULTS

In this section, we discuss the bulk features of the jet, including the experimentally observed jet front propagation, lofting trajectories. The pattern of sedimentation of particles is also examined. The results are compared with our theoretical model presented in Sec. II.

A. Bulk dynamics

The jet's front position, x_f, is tracked over time, t, beginning when the jet fluid first emanated from the source. Figure 7 shows the front position of the jet for different experiments having ambient densities, $\rho_a = 1.001\,\mathrm{g/cm^3}$ (top), $1.005\,\mathrm{g/cm^3}$ (middle), and $1.010\,\mathrm{g/cm^3}$ (bottom), and particle sizes, $d_p = 30\,\mu$m (left) and $d_p = 60\,\mu$m (right), respectively. The front slowed as it advanced along the tank bottom in all experiments. In most lofting experiments, the front advancement stops much before the end of the tank. However, in some lofting jet cases, the front reached the end of the tank due to the low buoyancy of the jet and low settling rate of particles. This behavior is expected whenever there is a small difference between ambient and interstitial fluid density. However, lofting occurred for larger particles even with small ambient density [Fig. 7(b)] due to the rapid settling of

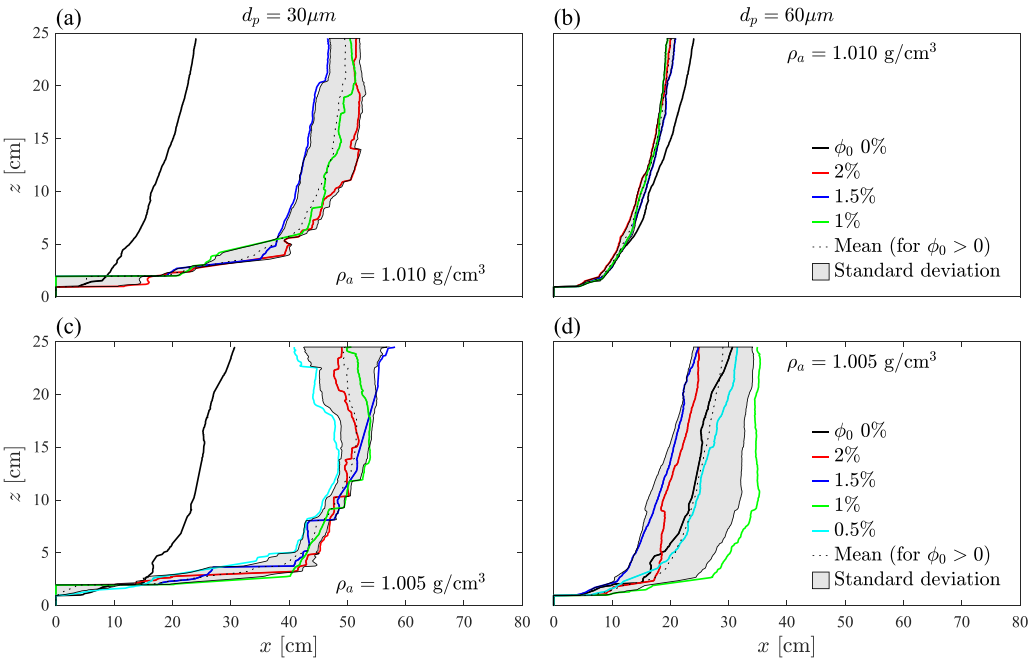

FIG. 8. Centerline trajectories (from experiments) of the jet with shaded area marking the error limits for experiments with particles. Panels (a) and (c) (left column) correspond to $d_p = 30\,\mu$m, and panels (b) and (d) (right column) refer to $d_p = 60\,\mu$m. Panels (a) and (c) have the same parameters and color schemes as panels (b) and (d), respectively.

particles. For the cases with $\rho_a = 1.005\,\text{g/cm}^3$ and $\rho_a = 1.010\,\text{g/cm}^3$ the jet lofted for $d_p = 30\,\mu$m and $d_p = 60\,\mu$m, and for all the prescribed particle concentrations, ϕ_0, but with $d_p = 60\,\mu$m the jet lofted closer to source compared to $d_p = 30\,\mu$m.

The edge of the jet was determined using 20% intensity thresholding of the maximum intensity captured by the camera. Subsequently, both edges were diagonally averaged to obtain the jet centerline trajectories, as shown in Fig. 8 for different values of ϕ_0 and ρ_a. In experiments with $\rho_a = 1.010\,\text{g/cm}^3$ shown in Fig. 8(a), a clear difference is observed between the case of no particles and with $d_p = 30\,\mu$m. The particle-bearing lofting jet propagated further downstream before becoming positively buoyant and lofting. When $\phi_0 > 0.2\%$, the lofting was delayed, and the trajectories were similar, falling within the error limits. A corresponding similar trend for $d_p = 30\,\mu$m was visible for $\rho_a = 1.005\,\text{g/cm}^3$, as shown in Fig. 8(c). With a larger particle diameter of $d_p = 60\,\mu$m, we observed that the lofting mechanism was the same as that of the no particle case, as shown in Figs. 8(b) and 8(d). This behavior can be attributed to the rapid settling of large size particles near the source. There is a reversing trend in the lofting jet trajectories for the case of $\rho_a = 1.005\,\text{g/cm}^3$ and $d_p = 30\,\mu$m, as shown in Fig. 8(c) wherein the averaged trajectories show changes in their path from advancing forward to backward. This is due to the development of a significant lag between the edges of the lofting jet caused by the dominant momentum forces compared to the case of relatively strong buoyant ambient fluid, $\rho_a = 1.010\,\text{g/cm}^3$ experiments. In general, we observe that the presence of particles and their size influence the lofting location irrespective of the concentration of particles.

B. Particle sedimentation

The sediment depth is measured using the light attenuation technique. Figures 9(a) and 9(b) show the sediment deposit pattern after the end of experiments 18 and 6, respectively, where $\phi_0 = 2\%$

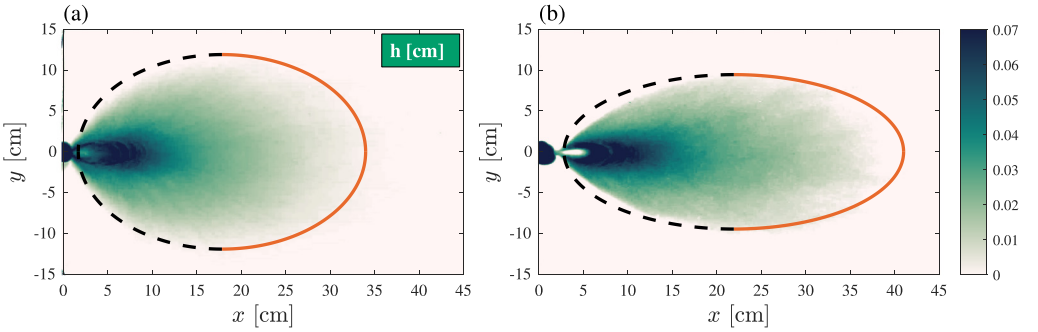

FIG. 9. Comparison of the sediment deposit at the end of experiments 18 and 6 [(a) and (b), respectively], which corresponds to same $\phi_0 = 2\%$. Panel (a) refers to the case of particle-bearing jet with $\rho_a = \rho_i$, and (b) is a particle-bearing lofting jet with $\frac{\rho_a - \rho_i}{\rho_a} = 0.0119$. The scale to the right shows the sediment depth in cm.

for both cases. Figure 9(a) shows a nonlofting jet having $\rho_a = \rho_i = 0.998\,\mathrm{g/cm^3}$ and Fig. 9(b) shows a lofting jet with $\rho_a = 1.010\,\mathrm{g/cm^3}$ and $\rho_i = 0.998\,\mathrm{g/cm^3}$. We observe that both the patterns displayed in Figs. 9(a) and 9(b) are elliptical but with different eccentricities. The orange curve drawn around the sediment indicates the approximate extent of the sediment. This is approximated by an ellipse with measured half-width, W_s^*, and half-length, L_s^* in which $L_s^* = X_m^* - X_{W_s}^*$ [see Eqs. (19) and (20) for their theoretical counterparts]. The analysis is performed using MatLab, which sets a threshold of maximum sediment extent where the sediment depth was 1% of the maximum value. The sediment pattern shows a higher eccentricity for the lofting jet than for the nonlofting case. Similar elongated deposits were also observed by Gladstone and Pritchard [5] for constant-volume and by Steel *et al.* [8] for constant-flux reversing buoyancy turbidity currents.

For comparison purposes, the measured half-width and half-length of the ellipse are compared with the theory in Fig. 10. We plot the ratio of experimental to theoretical values, L_s^*/L_s and W_s^*/W_s. For $\phi_0 > 0.2\%$, the values of L_s^*/L_s varies between 0.8 to 1.25 and the relative width W_s^*/W_s ranges from 0.5 to 2. The measured width was larger than predicted. This discrepancy is because the initial concentration of the particles, ϕ_0, also affects the sediment shape, whereas the theory suggests that W_s/L_s is only a function of α and C_d (see Sec. II D). Since high particle concentration results in a

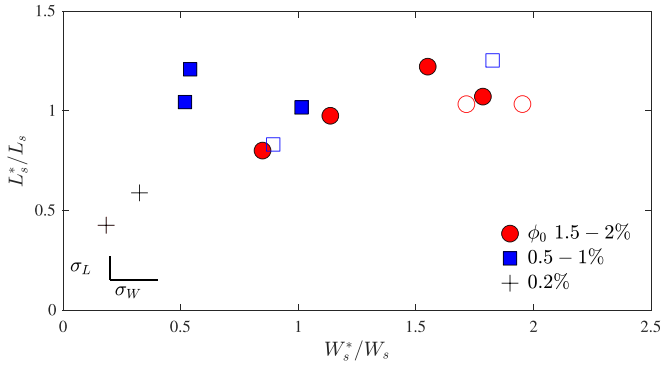

FIG. 10. The measured half-width, W_s^*, with the half-length, L_s^* of the elliptical shape sediment deposit (from experiments) normalized by the predicted theoretical half-width, W_s, with the half-length, L_s as given by Eqs. (19) and (20). σ_L and σ_W are the error limits of the experimental data. Open symbols corresponds to nonlofting experiments ($\rho_a = \rho_i$; see Table I).

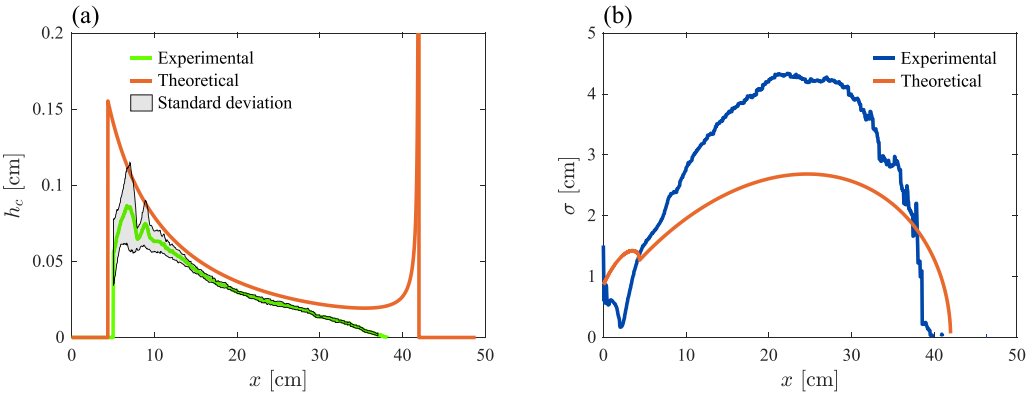

FIG. 11. (a) The sediment deposition depth, h_c along the jet centerline. The solid orange curve shows the theoretical predictions. (b) The standard deviation σ of the sediment deposit in the span-wise direction plotted along the jet direction. Both panels (a) and (b) correspond to experiment 6.

deeper deposit, particle deposition nonnegligibly influences bottom drag. But these dynamics are not included in the theory.

Figure 11(a) shows the centerline sediment depth, h_c, along the horizontal direction at $y = 0$. The green curve shows the measured sediment depth at the centerline, determined using the light attenuation technique, the gray-shaded region indicates the standard deviation. The theoretical prediction for $h_c(x)$ is shown by the orange curve in Fig. 11(a). It is found by putting $y = 0$ in Eq. (18). The predicted sediment depth is in satisfactory agreement with measurements until the predicted lofting point, beyond which the theory predicts the settling of excess sediment near the lofting point, thereby causing a spike in sediment depth. This spike occurs because the theory does not account for particles being carried upward by the lofting jet or for interactions between the jet and deposited sediments.

Figure 11(b) shows the experimental standard deviation, σ, of the spanwise extent of the sediment pattern at each streamwise location (blue curve). The measurement of σ is done by taking the sediment depth's standard deviation in the spanwise direction (along y). The theory does a reasonable job in qualitatively predicting the trends in σ and estimates the final position where sedimentation should stop. Overall, the qualitative match with experiments is satisfactory.

The characteristic height scale, $\overline{H}$, of the sediment is estimated by noting that the volume of particles injected during the time t_f of an experiment is given by $V = Q_0 t_f \phi_0$. The average area of the sediment can be assumed to be that of an ellipse, as shown by the dotted and orange curves in Fig. 9:

$$A = \pi W_s L_s \tag{23}$$

in which W_s is the minor axis of the ellipse and $(L_s = X_m - X_{W_m})$ is the major axis. Thus, assuming a loose-sphere packing fraction of $p_f = 0.56$, the mean height is predicted to be

$$\overline{H} = \frac{1}{p_f}\frac{V}{A} = \frac{Q_0 t_f \phi_0}{\pi p_f W_s L_s}. \tag{24}$$

The length where the bedload transport stops can be written as [Eq. (2.16) of Kapil *et al.* [19]]

$$L_m = \left(\frac{M_0}{g'_p d_p}\right)^{1/2}. \tag{25}$$

Figure 12 shows the maximum sediment deposit location l_0 at the centerline for various particle concentrations and ambient densities with particle diameter $d_p = 30\,\mu$m. The length predicting the

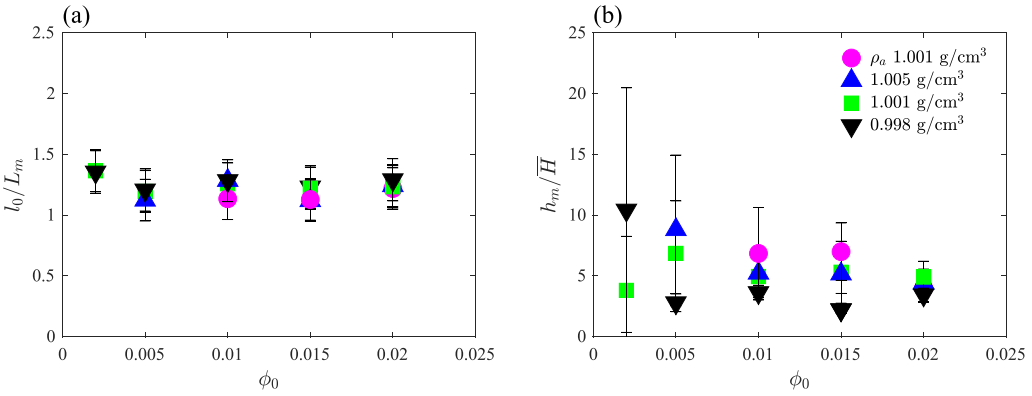

FIG. 12. (a) Distance, l_0, from virtual origin of the maximum sediment depth measured from experiments for varying ϕ and ρ_a given relative to scaling L_m. Symbols represent the different values of ambient density, ρ_a, for both (a) and (b). (b) Plot of measured maximum sediment depth h_m normalized by the mean depth $\overline{H}$ as given by Eq. (24). Vertical bars indicate the standard deviation near l_0 and h_m. The symbols in (a) are the same as those indicated in (b).

bedload transport, L_m, as given in Eq. (25), is used to scale this maximum location for all the experiments, as shown in Fig. 12(a). The measured maximum sediment depth, h_m at the centerline relative to $\overline{H}$ is shown in Fig. 12(b), plotted for all the particle fractions at different ambient densities and particle diameter $d_p = 30\,\mu$m.

Overall, we conclude that the theoretical predictions agree reasonably well with the experimental measurements of the lofting location, sediment pattern, and sediment deposit width, except for the experiments where the effect of sediment drag due to higher particle concentration is not accurately accounted for in theory. This work paves way for future investigation into the interesting phenomena of reversing buoyancy jets.

V. CONCLUSION

We examined the spreading and sedimentation dynamics of reversing buoyancy particle-bearing wall jets. The experiments and theory were presented for a range of parameters, namely the source momentum, M_0, volume flux, Q_0, particle volume fraction, ϕ_0, particle density, ρ_p, particle diameter, d_p, and buoyancy of interstitial fluid, $\rho_a - \rho_i$. The focus of the analysis was on the lofting location and particle deposition. The theoretical prediction for the lofting location was captured by including the suction force of the bottom wall acting on the jet, with a best-fit coefficient of suction found to be $C_s \simeq 20$. Drag at the bottom wall acted to bring the lofting location closer to the source. Compared with experiments, the best-fit coefficient of drag was $C_d \simeq 0.02$. The inner tear-drop shape at the start of deposition was captured using the Shields parameter with $\gamma_s = 0.3$. The elliptical outer extent of the deposit was captured by theory influenced by the enhanced settling parameter $\beta \simeq 5$. The maximum extent of sedimentation was governed primarily by the parameter $\gamma = 12$.

Experiments show that the sediment deposit in lofting experiments was more eccentric than in the nonlofting experiments. Compared to the experiment, our theory showed a satisfactory match in predicting the lofting location and the overall sediment deposition pattern.

A weakness of the theory is its six empirical parameters. However, every parameter represents a physical mechanism associated with the process of lofting and sediment deposition of the reversing buoyancy particle-bearing jets. Due to the experimental constraints, the study of deposition patterns was limited to $d_p \geqslant 30\,\mu$m. The effect of smaller diameter particles on the sedimentation and lofting location will be the focus of future work performed in a longer and wider tank.

ACKNOWLEDGMENTS

We thank the Shastri Indo-Canadian Institute for providing financial support for this research work in the form of Shastri Institutional Collaborative Research Grant (SICRG). M.K. is grateful for the funding support by University of Alberta during his stay there as an exchange graduate student.

[1] R. Sparks, R. Bonnecaze, H. Huppert, J. Lister, M. Hallworth, H. Mader, and J. Phillips, Sediment-laden gravity currents with reversing buoyancy, Earth Planet. Sci. Lett. **114**, 243 (1993).

[2] A. Hogg, H. Huppert, and M. Hallworth, Reversing buoyancy of particle-driven gravity currents, Phys. Fluids **11**, 2891 (1999).

[3] A. W. Woods and J. Kienle, The dynamics and thermodynamics of volcanic clouds: Theory and observations from the April 15 and April 21, 1990 eruptions of redoubt volcano, Alaska, J. Volcanol. Geotherm. Res. **62**, 273 (1994).

[4] B. E. Hürzeler, J. Imberger, and G. N. Ivey, Dynamics of turbidity current with reversing buoyancy, J. Hydraul. Eng. **122**, 230 (1996).

[5] C. Gladstone and D. Pritchard, Patterns of deposition from experimental turbidity currents with reversing buoyancy, Sedimentology **57**, 53 (2010).

[6] R. C. Y. Koh and N. H. Brooks, Fluid mechanics of waste-water disposal in the ocean, Annu. Rev. Fluid Mech. **7**, 187 (1975).

[7] T. C. Harris, A. J. Hogg, and H. E. Huppert, A mathematical framework for the analysis of particle-driven gravity currents, Proc. R. Soc. London A **457**, 1241 (2001).

[8] E. Steel, J. Buttles, A. R. Simms, D. Mohrig, and E. Meiburg, The role of buoyancy reversal in turbidite deposition and submarine fan geometry, Geology **45**, 35 (2017).

[9] O. E. Sequeiros, A. Cantelli, E. Viparelli, J. D. L. White, M. H. Garcia, and G. Parker, Modeling turbidity currents with nonuniform sediment and reverse buoyancy, Water Resour. Res. **45**, W06408 (2009).

[10] B. R. Sutherland and Y. S. D. Hong, Sedimentation from particle-bearing plumes in a stratified ambient, Phys. Rev. Fluids **1**, 074302 (2016).

[11] H. N. Mirajkar, S. Tirodkar, and S. Balasubramanian, Experimental study on growth and spread of dispersed particle-laden plume in a linearly stratified environment, Environ. Fluid Mech. **15**, 1241 (2015).

[12] D. D. Apsley and G. F. Lane-Serff, Collapse of particle-laden buoyant plumes, J. Fluid Mech. **865**, 904 (2019).

[13] G. Abraham, Jet diffusion in stagnant ambient fluid, Ph.D. thesis, Delft University of Technology, 1963.

[14] E. Hirst, Buoyant jets discharged to quiescent stratified ambients, J. Geophys. Res. (1896–1977) **76**, 7375 (1971).

[15] B. R. Morton, G. I. Taylor, and J. S. Turner, Turbulent gravitational convection from maintained and instantaneous sources, Proc. R. Soc. London A **234**, 1 (1956).

[16] G. H. Jirka, Integral model for turbulent buoyant jets in unbounded stratified flows. Part I: Single round jet, Environ. Fluid Mech. **4**, 1 (2004).

[17] J. Sharp and B. Vyas, The buoyant wall jet, Proc. Inst. Civ. Eng. **63**, 593 (1977).

[18] H. C. Burridge and G. R. Hunt, From free jets to clinging wall jets: The influence of a horizontal boundary on a horizontally forced buoyant jet, Phys. Rev. Fluids **2**, 023501 (2017).

[19] M. Kapil, B. R. Sutherland, and S. Balasubramanian, Spreading and sedimentation from bottom-propagating particle-bearing jets, J. Fluid Mech. **907**, A20 (2021).

[20] A. J. Cuthbertson, D. D. Apsley, P. A. Davies, G. Lipari, and P. K. Stansby, Deposition from particle-laden, plane, turbulent, buoyant jets, J. Hydraul. Eng. **134**, 1110 (2008).

[21] E. Ezhova, C. Cenedese, and L. Brandt, Dynamics of three-dimensional turbulent wall plumes and implications for estimates of submarine glacier melting, J. Phys. Oceanogr. **48**, 1941 (2018).

[22] H. A. Einstein, Deposition of suspended particles in a gravel bed, J. Hydr. Div. **94**, 1197 (1968).

[23] D. Martin and R. Nokes, Crystal settling in a vigorously convecting magma chamber, Nature (London) **332**, 534 (1988).
[24] R. Bonnecaze, H. Huppert, and J. Lister, Particle-driven gravity currents, J. Fluid Mech. **250**, 339 (1993).
[25] E. Kaminski, S. Tait, and G. Carazzo, Turbulent entrainment in jets with arbitrary buoyancy, J. Fluid Mech. **526**, 361 (2005).
[26] G. R. Hunt and P. F. Linden, Steady-state flows in an enclosure ventilated by buoyancy forces assisted by wind, J. Fluid Mech. **426**, 355 (2001).
[27] R. J. Munro and S. B. Dalziel, Attenuation technique for measuring sediment displacement levels, Exp. Fluids **39**, 602 (2005).